Microbial Reduction of Metal-Organic Frameworks Enables Synergistic Chromium Removal

Sarah K. Springthorpe[1], Christopher M. Dundas[2], Benjamin K. Keitz[2]*

[1]Department of Chemistry, University of Texas at Austin, Austin, TX 78712;

[2]McKetta Department of Chemical Engineering, University of Texas at Austin, Austin, TX 78712;

*To whom correspondence should be addressed. Email: keitz@utexas.edu

Abstract

Microbial interactions with redox-active materials are ubiquitous in geochemical cycling and bioelectrochemical devices, but the biotic-abiotic interface has proven challenging to study due to the structural complexity of mineral substrates. In contrast, metal-organic frameworks are a class of porous materials that exhibit well-defined structures, extensive chemical tunability, and high crystallinity. Here, we report that metal-organic frameworks can support the growth of the electroactive bacterium *Shewanella oneidensis*. Specifically, we demonstrate that Fe(III)-containing frameworks, MIL-100 and Fe-BTC, can be reduced by the bacterium via its extracellular electron transport pathways and that reduction rate/extent is tied to framework structure, surface area, and particle morphology. In a practical application, we show that cultures containing *S. oneidensis* and reduced frameworks can remediate lethal concentrations of Cr(VI), and that pollutant removal exceeds the performance of either component in isolation or bioreduced iron oxides. Repeated cycles of Cr(VI) dosing had little effect on bacterial viability or Cr(VI) adsorption capacity, demonstrating that the framework confers protection to the bacteria and that no regenerative step is needed for continued bioremediation. In sum, our results show that the study of microbial-material interactions can be extended to metal-organic frameworks and suggest that these materials may offer a promising alternative to metal oxides in applications seeking to combine the advantages of bacterial metabolism and synthetic materials.

Introduction

Redox-active minerals support the growth of metal-reducing and oxidizing microorganisms in anaerobic environments(*1*). These microbial-mineral interactions play a key role in biogeochemical processes, including the nitrogen and carbon cycles(*2*, *3*), as well as emerging technologies like microbial fuel cells(*4*) and bioremediation(*5*). Unfortunately, the study of microbe-mineral interactions is challenging due to the structural and thermodynamic complexity

of many metal oxides(*6*, *7*). For example, iron oxides exists in several different mineral forms with variable crystallinities, surface areas, and formal oxidation-reduction potentials(*8*). Specific iron oxide polymorphs can also be difficult to prepare under laboratory conditions and even relatively accessible structures, such as ferrihydrite (Fe_2O_3), are recalcitrant to structural characterization(*9*). Overall, the complexity of metal oxides makes it challenging to elucidate how bioelectronic physiology adapts to changes in material properties.

An emerging alternative to metal oxides in many applications are metal-organic frameworks. Relative to metal oxides, these materials generally exhibit higher surface areas and superior crystallinity. More importantly, metal-organic frameworks facilitate the development of highly tunable structure-function relationships since properties such as pore size, linker identity, and metal node can be varied independently of one another(*10*). As a result, they have seen an explosion in interest across several fields, including gas separations(*11*), catalysis(*12*), drug delivery(*13*), and environmental remediation(*14*). However, despite their advantages over metal oxides and potential presence in nature(*15*), metal-organic frameworks have not been examined as substrates for the growth of metal-reducing or oxidizing microorganisms.

Here, we demonstrate that the iron-based metal-organic frameworks Fe-BTC (BTC = 1,3,5-benzenetricarboxylate), $Fe_3O(BTC)_2(OH)\cdot nH_2O$ (MIL-100), and $Fe_3O[(C_2H_2(CO_2)_2]_3(OH)\cdot nH_2O$ (MIL-88A) can serve as respiratory electron acceptors for the metal-reducing bacteria *Shewanella oneidensis* MR-1 (Figure 1). We also show that bacterial growth and metal reduction rate are intimately tied to framework structure, crystallinity, and surface area. Similar to growth on metal oxides, reduction could be influenced with exogenous flavins and was governed by the metal reduction (Mtr) pathway in *S. oneidensis* (Figure 1a). Finally, in a practical application, we show that MR-1 and MIL-100 synergistically facilitate the reduction and adsorption of Cr(VI) at rates and capacities that exceed those of biotic metal oxides or abiotic frameworks. When operated together, the combination of MR-1 and MIL-100 protected the bacteria from repeated challenges with lethal concentrations of Cr(VI) and required no separate regenerative step. Overall, our results highlight the ability of metal-organic frameworks to support bacterial growth in a structure dependent manner and demonstrate how the advantages of these materials can be leveraged for heavy metal adsorption when coupled to bacterial metabolism.

Results

S. oneidensis MR-1 growth on metal-organic frameworks

First, we examined whether MR-1 could use iron-based metal-organic frameworks as respiratory substrates for cell growth. We prepared Fe-BTC, MIL-100, and MIL-88A under standard conditions and verified their structures via powder X-ray diffraction (PXRD) (Figure S1). Framework stability under typical culture conditions in the absence of bacteria was confirmed by monitoring Fe(III) and fumarate leaching, as well as PXRD (Figure S1). MIL-100 and Fe-BTC maintained structural integrity while MIL-88A exhibited a slight, but detectable, change in structure. To monitor the growth of MR-1, each framework was suspended in *Shewanella* Basal Medium (SBM) containing lactate as a carbon source and inoculated with anaerobically pregrown MR-1. While OD_{600} is readily used to measure bacterial growth on soluble substrates, quantification of growth on an insoluble substrate can be problematic due to interference from the material and confounding effects of biofilm development and adsorption of planktonic cells (*16*). Indeed, we measured no increase in MR-1 OD_{600} in the presence of any of our iron-based frameworks. Measuring growth using the biofilm stain crystal violet also proved infeasible since frameworks non-specifically adsorbed the dye in the absence of cells. Ultimately, we used the auto-fluorescence of secreted flavins (flavin mononucleotide, riboflavin, flavin adenine dinucleotide) to quantify cell growth and draw comparisons between frameworks. Although less common than OD_{600}, previous studies have shown that flavin auto-fluorescence accurately tracks cell growth at low cell densities(*17*). We confirmed that this was also true for MR-1 under anaerobic conditions with both soluble (fumarate) and insoluble (ferrihydrite) acceptors (Figure 2a, Figure S2). Furthermore, the presence of metal-organic frameworks did not interfere with flavin auto-fluorescence (Figure S2).

Having demonstrated that auto-fluorescence could be used as a proxy for cell growth, we examined the ability of MR-1 to grow on Fe-BTC, MIL-100, and MIL-88A. Cultures grown on MIL-100 exhibited a significant increase in fluorescence over time (Figure 2a). We corroborated that this increase was due to cell growth by directly assaying MR-1 colony forming units (CFUs), which also increased over the same time period (Figure 2b). Significant increases in fluorescence were also observed for MR-1 growing on Fe-BTC. Conversely, MR-1 in the presence of MIL-88A showed no increase in auto-fluorescence over time, implying a lack of growth. Together, these results demonstrate that MR-1 is able to grow on some iron-based metal-organic frameworks and that cell growth is tied to framework structure.

Microbial growth is coupled to framework reduction

Under anaerobic conditions and in the absence of a soluble electron acceptor, growth of MR-1 must be coupled to Fe(III) reduction. Thus, we analyzed the extent of Fe(III) reduction in each metal-organic framework when it was used as a substrate for MR-1 growth. Abiotic controls showed no reduction in any of the frameworks over the course of the experiment (up to 144 hours). In contrast, significant amounts of Fe(II) were observed when MR-1 was grown on MIL-100 and Fe-BTC (Figure 3a). For Fe-BTC, MR-1 reduced 1.9±0.3 mM Fe(III) before plateauing after 72 h. The largest extent of reduction was observed with MIL-100, with Fe(II) concentrations reaching 5.1±0.6 mM Fe(II) after 144 h. Assuming all Fe(III) in MIL-100 was reduced, the theoretical maximum Fe(II) concentration would be 15 mM. Thus, our results indicate that MR-1 can access approximately a third of the Fe(III) in the MIL-100 structure. As expected from our growth experiments, a minimal amount of reduction was observed when a suspension of MIL-88A was inoculated with MR-1. The above results correspond to reduction rates of 48.4±0.7 $\mu M\ h^{-1}$ for MIL-100, 28.8±3.3 $\mu M\ h^{-1}$ for Fe-BTC, and 3.4±0.9 $\mu M\ h^{-1}$ for MIL-88A. For comparison, MR-1 grown on ferrihydrite showed a reduction rate of 5.6±1.6 $\mu M\ h^{-1}$, which is consistent with previous reports when normalized by initial OD_{600}(*18*). These data confirm that bacterial growth is associated with Fe(III) reduction and that both processes depend on framework structure.

Next, we investigated how the structural and morphological differences between our frameworks contributed to the observed variation in iron reduction rates. MIL-100 and Fe-BTC are closely related in molecular structure, with MIL-100 being more crystalline, as evidenced by its PXRD pattern. Interestingly, iron oxides with higher degrees of crystallinity are typically associated with slower Fe(III) reduction rates across the *Shewanella* genus(*19*, *20*). However, the extent of Fe(III) reduction by metal-reducing bacteria is also dependent on the interplay between particle size, extent of aggregation, and surface area. For both MR-1 and *Geobacter sulfurreducens*, bacterially accessible surface area, informed by extent of particle aggregation, influenced the reduction rate of hematite nanoparticles (*21*, *22*). Furthermore, it has been found that the interfacial contact between outer membrane cytochromes and iron oxides impacts reduction rates, with smaller particles unable to provide adequate contact for reduction(*23*). To determine if similar material features influenced the biological reduction of metal-organic frameworks, we examined the morphology of MIL-100, Fe-BTC, and MIL-88A using scanning electron microscopy (SEM). SEM images showed that MIL-100 and Fe-BTC were highly aggregated, while MIL-88A was comprised of small, well-defined crystals approximately the same size as MR-1 (Figure S3). Based on its small crystallite size, MIL-88A is unlikely to support biofilm

development. Although they are morphologically similar, MIL-100 and Fe-BTC vary significantly in accessible surface area. MIL-100 had the largest Langmuir surface area (2188 m^2g^{-1}) followed by Fe-BTC (1512 m^2g^{-1}), ferrihydrite (311 m^2g^{-1},(*24*)) and MIL-88A (130 m^2g^{-1}) (Table S1). These surface areas closely track our measured Fe(III) reduction rates. Overall, our results are consistent with previous studies of MR-1 growth on iron oxides and show that biotic metal-organic framework reduction is governed through a combination of particle morphology, framework structure, and accessible surface area.

Stability of metal-organic frameworks in the presence of MR-1

Next, we asked if Fe(III) reduction and metabolic activity from MR-1 negatively impacted the solution stability of the frameworks. Collecting PXRD patterns after bacterial growth, we found that MIL-88A eventually decomposed under biotic conditions. Curiously, even though MIL-88A decomposed, it did not release Fe(III) or fumarate to support bacterial growth. In contrast, MIL-100 showed good stability and crystallinity after exposure to MR-1 (Figure S4). This result indicates that MIL-100 remains intact during the reduction process. Despite the overall structural integrity of MIL-100 in the presence of MR-1, we confirmed that the bacteria are able to solubilize some iron in the framework. After 24 hours, the amount of Fe(II) in solution was 0.95 ± 0.06 mM, while total Fe(II) was 2.31 ± 0.12 mM (Figure S5). This result indicates that MR-1 can both directly reduce Fe(III) in MIL-100 and partially remove Fe(II/III) from the framework structure.

The Mtr pathway controls metal-organic framework reduction

The Mtr pathway in MR-1 is largely responsible for extracellular electron transport and interfacing with insoluble metal oxides(*18*). Specifically, the outer-membrane cytochromes MtrC and OmcA enable the terminal electron transfer step onto both soluble and insoluble metal species(*25*). Without these proteins, *S. oneidensis* shows attenuated respiration onto iron and graphene oxides(*26*). Thus, we investigated the role of these cytochromes on the reduction of MIL-100 and Fe-BTC. For both frameworks, an outer-membrane cytochrome deficient strain, Δ*mtrC*Δ*omcA*, showed minimal Fe(III) reduction relative to MR-1 (Figure 3b, Figure S6). *Escherichia coli* MG1655, which does not possess a homolog to MtrC or OmcA, was also unable to reduce MIL-100 or Fe-BTC (Figure S7). Together, these results confirm that the same biological pathways responsible for iron oxide reduction by *S. oneidensis* also play a key role in their reduction of metal-organic frameworks.

Exogenous flavins improve Fe(III) reduction in metal-organic frameworks

In addition to the Mtr pathway, MR-1 uses soluble redox shuttles (flavins) to transport reducing equivalents to metal oxides, with exogenously supplied flavins accelerating the rate of Fe(III) reduction(*27*). Similarly, we found that addition of 10 μM riboflavin to MR-1 cultures containing MIL-100 increased Fe(III) reduction rates and the total amount of Fe(II) (Figure 3c). In the presence of excess flavins, MR-1 could access approximately half of the Fe(III) in the MIL-100 framework. When grown on MIL-100, a strain lacking flavin export machinery (Δ*bfe*) showed a slight, but significant, decrease in Fe(III) reduction rate relative to MR-1 (Figure 3b). These results are consistent with previous studies where the Δ*bfe* strain exhibited a similar decrease in Fe(III) reduction compared to MR-1 when both were grown on ferrihydrite (*28*). Overall, our data indicate that flavins are important contributors to Fe(III) reduction in metal-organic frameworks.

Cr(VI) adsorption by microbially-reduced metal-organic frameworks

Microbial reduction of iron oxides and release of reactive Fe(II) plays a major role in water quality control and the transport of heavy metal contaminants(*29*). Metal-reducing bacteria, including MR-1, can also directly reduce various heavy metal species(*30*). As a result, metal-reducing bacteria, acting in conjunction with iron oxides, have been proposed for the bioremediation of highly oxidized and toxic contaminates, such as CrO_4^{-2} or $Cr_2O_7^{-2}$(*31*). Indeed, MR-1 can reduce up to 200 μM of Cr(VI) in a 24 h period(*32*). Biologically-reduced iron oxides have also shown promise in Cr(VI) removal by reductive adsorption(*31*). An alternative to bioremediation is the use of standard inorganic adsorbents, including activated carbons and metal-organic frameworks. Some metal-organic frameworks have also shown promise for Cr(VI) adsorption, but generally show slow adsorption kinetics and limited capacities(*33-35*). A more recent advance found that Cr(VI) adsorption could be dramatically improved by adding $FeSO_4$ to the metal-organic framework UTSA-74 (*14*). This result implies that, similar to the case with iron oxides, the presence of Fe(II) can enhance reductive adsorption of Cr(VI). Based on these results, we hypothesized that microbial reduction of metal-organic frameworks could exhibit a synergistic effect on Cr(VI) removal (Figure 4a).

In initial experiments, we grew MR-1 on each metal-organic framework for 24 hours and then challenged the culture with a single dose of Cr(VI). At initial Cr(VI) concentrations of 70 μM, all frameworks showed immediate removal of soluble Cr(VI) below the detection limit of the

diphenylcarbazide (DPC) assay (Figure 4b-d). Abiotic controls and biotic ferrihydrite (Figure 4e) showed minimal and slow Cr(VI) adsorption. In the case of MIL-100 and Fe-BTC, we found that Fe(III) reduction continued to take place after Cr(VI) addition, indicating that MR-1 was still viable under these conditions. Even though MIL-88A showed minimal Fe(III) reduction in the presence of MR-1, it was still enough to reductively adsorb the relatively small initial dose of Cr(VI). These results are a preliminary indication that there is a synergistic interaction between the frameworks and MR-1 that accelerates Cr(VI) reduction and adsorption.

Next, we challenged MR-1 growing on MIL-100 with increasing concentrations of Cr(VI) up to 1 mM (Figure 4f). After dosing with 0.5 mM Cr(VI), MR-1 and MIL-100 reduced all detectable Cr(VI) within minutes. Under these conditions, the total solution concentration of Cr, as measured by inductively coupled plasma – mass spectrometry (ICP-MS), fell below 10 ppm within minutes and reached ~1 ppm after 24 hours (Figure S8). Furthermore, Fe(III) reduction continued to take place after Cr(VI) addition, suggesting that MR-1 can survive normally toxic Cr(VI) concentrations in the presence of MIL-100. At 1 mM Cr(VI), MR-1 on MIL-100 showed almost complete reduction, but over a much longer time period, indicating that this concentration is approaching the limit of toxicity for our system.

Finally, we sought to distinguish biological reduction of Cr(VI) from framework-mediated reductive adsorption. As mentioned above, MR-1 can directly reduce Cr(VI) through the Mtr pathway. Alternatively, MR-1 could mediate Cr(VI) reduction through MIL-100. Overall, we found that biotic samples in the absence of MIL-100 showed significantly slower Cr(VI) reduction kinetics and were more sensitive to the initial Cr(VI) dose (Figure S9). For example, MR-1 challenged with 500 μM Cr(VI) was only able to reduce ca. 100 μM after 24 hours and entered death phase, as measured by OD_{600} (Figure S10). These results are consistent with previous reports indicating that 200 μM Cr(VI) is the upper limit for MR-1 survivability(*32*). We also measured reduced Cr(VI) adsorption kinetics for MR-1 grown on ferrihydrite. Notably, even at low initial Cr(VI) concentrations, biotic and abiotic ferrihydrite samples exhibited worse adsorption kinetics and capacities relative to all frameworks tested (Figure 4). If MR-1 was primarily responsible for Cr(VI) reduction, we would not expect the substrate to make a significant difference. Additionally, after MR-1 had reduced appreciable amounts of Fe(III) in ferrihydrite, there was not a corresponding decrease in Cr(VI), as would have been expected if Fe(II) alone was responsible for Cr(VI) reduction. Thus, our results support a synergistic interaction between MR-1 and MIL-100 that

enhances Cr(VI) reduction/adsorption kinetics and capacity relative to abiotic frameworks and MR-1 growing on iron oxides.

Repeated cycles of Cr(VI) with MR-1 reduced MIL-100

The majority of materials for Cr(VI) adsorption require a regeneration step using pH adjustments after saturation(*36*). Based on our initial Cr(VI) adsorption experiments involving MR-1 and MIL-100, we predicted that viable cells could metabolically regenerate the framework for continued Cr(VI) reduction and adsorption. To determine and compare the recyclability of MR-1-reduced materials, samples containing either MIL-100, ferrihydrite, or fumarate were reduced by MR-1 for 24 h before being challenged with 10 cycles of $[Cr(VI)]_0$=0.50 mM, once every 24 hours. For all additions to MR-1 growing on MIL-100, Cr(VI) was removed below the limit of detection within minutes (Figure 4g). The total amount of Cr(VI) reduced by MR-1 and MIL-100 was 78.7±0.1 mg g^{-1}, which represents a 125-fold increase over MIL-100 alone and compares favorably to other Cr(VI) adsorbents (Table S2). In contrast, the biotic and abiotic treatments with fumarate and ferrihydrite showed no appreciable Cr(VI) adsorption and the amount of Cr(VI) in solution increased after each new dose. We also investigated whether a microbially-reduced soluble iron source could aid in removal of Cr(VI). Indeed, we found that MR-1 grown on Fe(III)-citrate enabled instantaneous reduction after repeated cycles of 0.50 mM Cr(VI) (Figure S11). However, no precipitate was formed upon Cr(VI) reduction. Similar results were found for abiotic reduction of Cr(VI) by $FeCl_2 \cdot 4H_2O$, with no precipitate forming despite complete reduction. These results suggest that, under our pH operating conditions, Cr(III) can only be removed from solution in the presence of a sorbent material, such as MIL-100. After Cr(VI) cycling, we characterized MIL-100 using scanning transmission electron microscopy (STEM) and transmission electron microscopy (TEM). Abiotic and biotic samples were morphologically similar (Figure S12). In contrast, elemental mapping revealed that cycled abiotic MIL-100 was primarily composed of Fe with small amounts of Cr while cycled biotic MIL-100 contained significantly more Cr (Figure 4h-i). This result supports our solution-based measurements and confirms that metabolic reduction of MIL-100 significantly increases its overall capacity for Cr(VI) adsorption.

Our cycling data suggests that MR-1 growing on fumarate or ferrihydrite is quickly overwhelmed after repeated challenges with Cr(VI). Indeed, we observed no increase in OD_{600} in the fumarate samples following the first addition of Cr(VI), implying that the cells had entered death phase (Figure S10). In contrast, we measured an increase in Fe(II) over the course of the cycling experiment when MR-1 was grown on MIL-100. As expected, Fe(II) concentrations

decreased immediately after the addition of Cr(VI) but rebounded as viable cells continued to reduce Fe(III) (Figure S13). We did not measure a similar trend in Fe(III) reduction for MR-1 grown on ferrihydrite that was repeatedly challenged with Cr(VI) (Figure S13). We also verified the observed trends in Fe(III) reduction during Cr(VI) cycling by directly assaying cell viability. Following the final Cr(VI) addition, the MIL-100 sample formed a lawn after an aliquot was plated on LB agar and grown aerobically overnight, indicating viable bacteria remained after Cr(VI) cycling. In contrast, abiotic samples, biotic ferrihydrite samples, and biotic fumarate samples showed no growth on LB agar plates (Figure S14). Together, these results demonstrate that MIL-100 both effectively protects MR-1 from cytotoxic Cr(VI) concentrations and synergistically enables Cr(VI) adsorption with maximum rates and capacities that greatly exceed those of biotic metal oxide or abiotic metal-organic frameworks.

Discussion

While previously limited to metal oxides, noble metals, and other electrode materials, we demonstrated that the study of microbial-material interactions can be extended to metal-organic frameworks. The major advantage of these materials is their synthetic tunability, which may allow for improved study of the microbial-material interface. For example, metal-organic frameworks can be constructed from a variety of biologically-relevant metal nodes, including iron, manganese, chromium, and cobalt(*10*). The pore size can also be tuned, potentially controlling the diffusion of flavins and other redox shuttles in the framework. Conceivably, the organic linker or other framework components could also be modified to act as secondary electron acceptors. We showed that MIL-88A, which contains fumarate, does not promote the growth of MR-1, which is expected since fumarate reductase is periplasmic. However, alternative substrates that accept reducing equivalents from outer membrane reductases could also be incorporated into frameworks. For example, frameworks such as those containing DMSO (Zn_2-(4,4'-Ethyne-1,2-diyldibenzoate)$_2$(DMSO)$_2$]·1.6H_2O)(*37*), porphyrins (PCN-222)(*38*), or conductive linkers (Co_2TTFTB; TTFTB = tetrathiafulvalene tetrabenzoate)(*39*) could potentially support microbial growth. The PCN-222 framework is of particular interest as the metal center of the porphyrin linker can be exchanged without change in overall structure and it is highly stable in water(*38*).

The major limitation of applying metal-organic frameworks as microbial growth substrates is their general instability under aqueous conditions. To counteract this, we examined water stable frameworks and also note that there are significant efforts to develop additional frameworks with enhanced water stability(*40*). Nevertheless, the aqueous stability of a specific framework must be

carefully scrutinized before it is selected as a substrate for microbial growth. For example, we found that stepanovite, a naturally-occurring metal-organic framework mineral, could also support the growth of MR-1, but that this effect was due to dissolution of the framework (Figure S15). Ultimately, utilization of water-stable frameworks possessing well-defined structures could potentially reduce the impact of abiotic material effects, such as phase or polymorph changes. This characteristic, combined with their synthetic tunability, should position metal-organic frameworks as useful tools for probing material effects on microbial physiology and improving the design of applications that exploit these relationships.

In one potential application, we showed that MR-1 operates synergistically with MIL-100 to reduce and adsorb significant amounts of Cr(VI). Notably, the high adsorption capacity of MIL-100 shielded the bacteria from repeated Cr(VI) challenges while analogous materials (ferrihydrite) provided no protection. The overall Cr capacity for MR-1 combined with MIL-100 was 79 mg g^{-1}, which exceeds the capacity of abiotic MIL-100 by two orders of magnitude. Moreover, since Fe(III) is continually reduced by MR-1, then reoxidized after Cr(VI) addition, the theoretical capacity is only limited by the amount of lactate in culture medium. Assuming all initial lactate is consumed by MR-1 under our operating conditions, the theoretical maximum capacity of Cr(VI) reduction and adsorption is 420 mg g^{-1}. Our results with MIL-100 also suggest that other redox-active frameworks could see a similar increase in Cr(VI) adsorption capacity when combined with MR-1. Alternatively, frameworks could support growth of metal-reducing bacteria to synergistically remediate other environmental pollutants like U(VI)(*41*) or could support syntrophic cocultures of different bacterial species. For example, iron oxides can serve as mediators of electron transfer between methanogens and *G. sulfurreducens* (*42*, *43*); iron-based metal-organic frameworks, including MIL-100, could play a similar role. Finally, metal-organic frameworks may be exciting materials to include in microbial fuel cells since their large surface areas, porosity, and ability to support bacterial growth may translate into performance improvements in these bioelectrochemical devices(*4*).

In conclusion, we showed that iron-based metal-organic frameworks can support the growth of the dissimilatory metal-reducing bacteria *S. oneidensis* via iron reduction. Both growth and rates of iron reduction were dependent on framework crystallinity, surface area, and particle morphology. Additionally, MR-1 growth was dependent on soluble redox shuttles (flavins) and the Mtr pathway. Finally, MR-1 and MIL-100 synergistically reduced and adsorbed Cr(VI) at rates and capacities that exceeded other biotic and abiotic systems. Overall, our results suggest that metal-

organic frameworks may be leveraged as unique tools to provide fundamental insights into biological electron transport and to enhance applications that rely on these pathways.

Materials and Methods

Synthesis of metal-organic frameworks and iron oxides

MIL-100 was synthesized by first dissolving H_3BTC (1.68 g, 7.6 mmol) and NaOH (0.91 g, 22.8 mmol) in 24 mL H_2O. This solution was added dropwise to $FeCl_2{\cdot}4H_2O$ (2.26 g, 11.4 mmol) dissolved in 97 mL H_2O and stirred for 24 h at room temperature/ambient conditions. The precipitate was isolated, washed with water and ethanol, and then dried at room temperature/ambient conditions(*44*). Fe-BTC was synthesized by dissolving H_3BTC (0.263 g, 1.2 mmol) and NaOH (0.15 g, 3.8 mmol) in 10 mL of H_2O. This solution was added dropwise to $FeCl_3{\cdot}6H_2O$ (0.513 g, 1.9 mmol) dissolved in 10 mL H_2O and stirred for 10 min at room temperature/ambient conditions. The precipitate was isolated, washed with water and ethanol, and then dried at room temperature/ambient conditions(*45*). MIL-88A was synthesized by stirring a solution of fumaric acid (0.97 g, 8.4 mmol) and $FeCl_3{\cdot}6H_2O$ (2.27 g, 8.4 mmol) in 42 mL of H_2O for 1 h before transferring to a Teflon-lined steel autoclave (Parr). The reactor was heated at 65 °C for 12 h and then cooled down to room temperature. Precipitate from inside the reactor was subsequently washed with ethanol and water, then dried at 120 °C for 10 h(*46*). Ferrihydrite was synthesized by adding 1M NaOH dropwise to $FeCl_3{\cdot}6H_2O$ (5.4 g, 20.0 mmol) dissolved in 100 mL H_2O until the pH reached ~7.5. The solid was isolated by centrifugation, washed with water, and lyophilized immediately following washing for 48 h(*24*). Stepanovite was synthesized by stirring red hematite (1.5 g, 9.5 mmol), NaOH (0.38 g, 9.5 mmol), and magnesium oxide (0.38, 9.5 mmol) in 30 mL of 10% w/v oxalic acid solution for 15 h. Single crystals were obtained by filtering and storing the solution at 4 °C for 24 h. Stepanovite powder used for MR-1 reduction was obtained by evaporating the solution after filtration using a rotary evaporator (85 °C, 45 rpm, low vacuum) (*15*).

Strains and culture conditions

All anaerobic cultures and experiments were performed inside a humidified Coy anaerobic chamber (3% H_2/balance N_2 atmosphere). *S. oneidensis* MR-1 was obtained from ATCC® (700550™). Mutant strains, Δ*mtrC*Δ*omcA* and Δ*bfe*, were generously provided by JA Gralnick

(University of Minnesota, Minneapolis, MN). For anaerobic pregrowths, all strains were cultured in SBM buffered with 100 mM HEPES and supplemented with 0.05% casamino acids and 0.5% Wolfe's mineral mix (*47*). The medium was adjusted to a pH of ~7.2. For pregrowth, sodium lactate (20 mM) and sodium fumarate (40 mM) were added as the carbon source and an electron acceptor, respectively. Once the bacteria reached stationary phase (ca. 18 h), they were pelleted by centrifugation (6000 x g; 20 min) and washed with SBM two times. A final addition of SBM was added to dilute the cells to OD_{600}=0.2.

Growth of MR-1 on metal-organic frameworks and iron oxides

Growth of MR-1 on the metal-organic frameworks was measured by CFU counting and by auto-fluorescence. For CFU counting, an aliquot of the culture suspension was removed and serially diluted (10^0-10^{-7}). Each dilution (100 μL) was plated onto LB agar plates using sterile glass beads and incubated aerobically at 30 ºC overnight. Individual colonies on each plate were counted and the initial concentration of MR-1 was calculated. For the auto-fluorescence assay, 250 μL of the culture suspension was removed, gently spun down to pellet the material, and the supernatant was transferred to a 96-well plate. Fluorescence was measured with an excitation/emission of 485/528 nm using a BMG LabTech CLARIOstar Monochromator Microplate Reader.

Reduction of metal-organic frameworks and ferrihydrite

Reduction of the metal-organic frameworks and ferrihydrite by MR-1 was tested by measuring Fe(II) concentrations in the cultures over time. Cultures containing 20 mM sodium lactate and either MIL-100, Fe-BTC, MIL-88A, or ferrihydrite ($[Fe(III)]_0$=15 mM) in fresh SBM were prepared anaerobically and then inoculated with the washed MR-1 to OD_{600}=0.002. Abiotic samples were prepared with the materials in SBM with lactate but with no cells. The cultures were incubated anaerobically at 30 °C for 144 h. At each time point, the material substrates were suspended before removing an aliquot from the culture. Each aliquot was mixed with 6 M HCl in a 1:1 ratio, until full dissolution of the framework or oxide occurred. Then, the sample was diluted with 1 M HCl in a 1:1 ratio and analyzed for Fe(II) using the ferrozine assay(*48*). The ferrozine assay was performed by mixing 15 μL of the diluted sampled with 235 μL of ferrozine solution in a 96-well plate. Absorbance was measured at 562 nm using a microplate reader. Ferrozine solution consisted of ferrozine (45 mg, 87 μmol) and ammonium acetate (22.5 g, 0.29 mol) in 45

mL H_2O. A similar protocol was followed for reduction of the frameworks by Δ*mtrC*Δ*omcA* and Δ*bfe*.

Cr(VI) adsorption to MR-1 reduced metal-organic frameworks and ferrihydrite

Cr(VI) removal was tested using metal-organic frameworks or ferrihydrite that had been reduced by MR-1 for 24 h. Cultures containing MIL-100 ($[Fe(III)]_0$=15 mM) and 20 mM lactate in SBM were inoculated with MR-1 to OD_{600}=0.002, as previously described. After 24 h, $K_2Cr_2O_7$ was added to each of the cultures ($[Cr(VI)]_0$=70 μM) and Fe(II) concentrations were analyzed. Cr(VI) concentration in the supernatant was analyzed using the DPC assay (*49*). The DPC assay was performed by mixing 15 μL of sample with 235 μL of DPC solution in a 96-well plate. Absorbance was measured at 540 nm in a microplate reader. DPC solution consisted of DPC (12.5 mg, 103 μmol) in a mixture of 0.5 M H_2SO_4 (10 mL) and acetone (10 mL). MIL-100 was tested with higher concentrations of Cr(VI) (0.25, 0.50, and 1 mM) using the same procedure.

Cr(VI) cycling

Cr(VI) removal from a supernatant was tested over ten cycles with MR-1 reduced MIL-100, ferrihydrite, and fumarate. MIL-100, ferrihydrite, and fumarate were biotically reduced for 24 h and $K_2Cr_2O_7$ was added to each culture ($[Cr(VI)]_0$=0.50 mM). Every 24 h, $K_2Cr_2O_7$ ($[Cr(VI)]_0$=0.50 mM) was added, with ten total additions occurring. Fe(II) concentration and Cr(VI) concentration in the supernatant were monitored as previously described. To determine cell viability, aliquots of each sample (100 μL) were plated on LB agar plates 24 h after the last Cr(VI) addition and cells were grown aerobically at 30 ºC overnight. Following cycling, cycled samples were washed in fresh H_2O and then dried anaerobically. Prior to STEM imaging, the samples were suspended in ethanol (500 μL) and dropcast on TEM grids. STEM imaging and electron mapping of Fe and Cr was performed using a JOEL 2010F Transmission Electron Microscope.

Supplementary Materials

Supporting figures and additional methods can be found in the Supplementary Materials.

Materials and Methods

Figure S1. Metal-organic framework structural characterization.

Figure S2. Auto-fluorescence measurements.

Figure S3. Metal-organic framework morphology.

References

1. L. Shi, H. Dong, G. Reguera, H. Beyenal, A. Lu, J. Liu, H-Q. Yu, J. K. Fredrickson, Extracellular electron transfer mechanisms between microorganisms and minerals. *Nat Rev Micro*. **14**, 651–662 (2016).

2. M. Vargas, K. Kashefi, E. L. Blunt-Harris, D. R. Lovley, Microbiological evidence for Fe(III) reduction on early Earth. *Nature*. **395**, 65–67 (1998).

3. A. Tagliabue, A. R. Bowie, P. W. Boyd, K. N. Buck, K. S. Johnson, M. A. Saito, The integral role of iron in ocean biogeochemistry. *Nature*. **543**, 51–59 (2017).

4. B. E. Logan, Exoelectrogenic bacteria that power microbial fuel cells. *Nat Rev Micro*. **7**, 375–381 (2009).

5. K. Rabaey, R. A. Rozendal, Microbial electrosynthesis — revisiting the electrical route for microbial production. *Nat Rev Micro*. **8**, 706–716 (2010).

6. M. F. Hochella, S. K. Lower, P. A. Maurice, R. L. Penn, N. Sahai, D. L. Sparks, B. S. Twinning, Nanominerals, Mineral Nanoparticles, and Earth Systems. *Science*. **319**, 1631–1635 (2008).

7. A. Navrotsky, L. Mazelna, J. Majzlan, Size-driven structural and thermodynamic complexity in iron oxides. *Science*. **319**, 1635–1638 (2008).

8. M. Sander, T. B. Hofstetter, C. A. Gorski, Electrochemical Analyses of Redox-Active Iron

Minerals: A Review of Nonmediated and Mediated Approaches. *Environ. Sci. Technol.* **49**, 5862–5878 (2015).

9. F. M. Michel, L. Ehm, S. A. Antao, P. L. Lee, P. J. Chupas, G. Liu, D. R. Strongin, M. A. A. Schoonen, B. L. Phillips, J. B. Parice, The structure of ferrihydrite, a nanocrystalline material. *Science*. **316**, 1726–1729 (2007).

10. M. O'Keeffe, O. M. Yaghi, Deconstructing the Crystal Structures of Metal–Organic Frameworks and Related Materials into Their Underlying Nets. *Chem. Rev.* **112**, 675–702 (2011).

11. T. M. McDonald, J. A. Mason, X. Kong, E. D. Bloch, G. Gygi, A. Dani, V. Crocella, F. Giordanino, S. O. Odoh, W. S. Drisdell, B. Vlaisavljevich, A. L. Dzubak, R. Poloni, S. K. Schnell, N. Planas, K. Lee, T. Pascal, L. F. Wan, D. Prendergast, J. B. Neaton, B. Smit, J. B. Kortright, L. Gagliardi, S. Bordiga, J. A. Reimer, J. R. Long, Cooperative insertion of CO2 in diamine-appended metal-organic frameworks. *Nature*. **519**, 303–308 (2015).

12. M. Ranocchiari, J. A. V. Bokhoven, Catalysis by metal–organic frameworks: fundamentals and opportunities. *Phys. Chem. Chem. Phys.* **13**, 6388–10 (2011).

13. P. Horcajada, R. Gref, T. Baati, P. K. Allan, G. Maurin, P. Couvreur, G. Ferey, R. E. Morris, C. Serre, Metal–Organic Frameworks in Biomedicine. *Chem. Rev.* **112**, 1232–1268 (2011).

14. M. B. Luo, Y. Y. Xiong, H. Q. Wu, X. F. Feng, J. Q. Li, F. Luo, The MOF +Technique: A Significant Synergic Effect Enables High Performance Chromate Removal. *Angew. Chem. Int. Ed.* **56**, 16376–16379 (2017).

15. I. Huskic, I. V. Pekov, S. V. Krivovichev, T. Friscic, Minerals with metal-organic framework structures. *Science Advances*. **2**, e1600621–e1600621 (2016).

16. K. O. Duedu, C. E. French, Data for discriminating dead/live bacteria in homogenous cell suspensions and the effect of insoluble substrates on turbidimetric measurements. *Data in Brief*. **12**, 169–174 (2017).

17. I. Mihalcescu, M. Van-Melle Gateau, B. Chelli, C. Pinel, J.-L. Ravanat, Green autofluorescence, a double edged monitoring tool for bacterial growth and activity in micro-plates. *Phys. Biol.* **12**, 066016–12 (2015).

18. D. Coursolle, J. A. Gralnick, Modularity of the Mtr respiratory pathway of Shewanella oneidensis strain MR-1. *Molecular Microbiology*. **55**, 995–1008 (2010).

19. X. Li, T. Liu, F. Li, W. Zhang, S. Zhou, Y. Li, Reduction of structural Fe(III) in oxyhydroxides by Shewanella decolorationis S12 and characterization of the surface properties of iron minerals. *J Soils Sediments*. **12**, 217–227 (2011).

20. H. Tan, O. K. Ezekoye, J. van der Schalie, M. W. Horn, A. Lakhtakia, J. Xu, W. D. Burgos, Biological Reduction of Nanoengineered Iron(III) Oxide Sculptured Thin Films. *Environ. Sci. Technol.* **40**, 5490–5495 (2006).

21. B. Yan, B. A. Wrenn, S. Basak, P. Biswas, D. E. Giammar, Microbial Reduction of Fe(III)

in Hematite Nanoparticles by Geobacter sulfurreducens. *Environ. Sci. Technol.* **42**, 6526–6531 (2008).

22. S. Bose, M. F. Hochella, Y. A. Gorby, D. W. Kennedy, D. E. McCready, A. S. Madden, B. H. Lower, Bioreduction of hematite nanoparticles by the dissimilatory iron reducing bacterium Shewanella oneidensis MR-1. *Geochimica et Cosmochimica Acta*. **73**, 962–976 (2009).

23. J. Liu, C. I. Pearce, L. Shi, Z. Wang, Z. Shi, E. Arenholz, K. M. Rosso, Particle size effect and the mechanism of hematite reduction by the outer membrane cytochrome OmcA of Shewanella oneidensis MR-1. *Geochimica et Cosmochimica Acta*. **193**, 160–175 (2016).

24. M. Villacis-Garcia, M. Ugalde-Arzate, K. Vaca-Escobar, M. Villalobos, R. Zanella, N. Martinez-Villegas, Laboratory synthesis of goethite and ferrihydrite of controlled particle sizes. *Boletin de la Sociedad Geologica Mexicana*. **67**, 433–446 (2015).

25. D. Coursolle, D. B. Baron, D. R. Bond, J. A. Gralnick, The Mtr Respiratory Pathway Is Essential for Reducing Flavins and Electrodes in Shewanella oneidensis. *Journal of Bacteriology*. **192**, 467–474 (2009).

26. Y. Jiao, F. Qian, Y. Li, G. Wang, C. W. Saltikov, J. A. Gralnick, Deciphering the Electron Transport Pathway for Graphene Oxide Reduction by Shewanella oneidensis MR-1. *Journal of Bacteriology*. **193**, 3662–3665 (2011).

27. E. Marsili, D. Baron, I. D. Shikhare, D. Coursolle, J. A. Gralnick, D. R. Bond, Shewanella secretes flavins that mediate extracellular electron transfer. *Proceedings of the National Academy of Sciences*. **105**, 3968–3973 (2008).

28. N. J. Kotloski, J. A. Gralnick, Flavin Electron Shuttles Dominate Extracellular Electron Transfer by Shewanella oneidensis. *mBio*. **4**, 1–4 (2013).

29. K. H. Nealson, J. Scott, M. Dworkin, S. Falkow, E. Rosenberg, K.-H. Schleifer, E. Stackebrandt, Eds. (Springer New York, New York, NY, ed. 3, 2006), vol. 6, pp. 1133–1151.

30. H. H. Hau, J. A. Gralnick, Ecology and Biotechnology of the Genus Shewanella. *Annu. Rev. Microbiol.* **61**, 237–258 (2007).

31. D. R. Brookshaw, V. S. Coker, J. R. Lloyd, D. J. Vaughan, R. A. D. Pattrick, Redox Interactions Between Cr(VI) and Fe(II) in Bioreduced Biotite and Chlorite. *Environ. Sci. Technol.* **48**, 11337–11342 (2014).

32. S. M. Belchik, D. W. Kennedy, A. C. Dohnalkova, Y. Wang, P. C. Sevinc, H. Wu, Y. Lin, H. P. Lu, J. K. Fredrickson, Extracellular Reduction of Hexavalent Chromium by Cytochromes MtrC and OmcA of Shewanella oneidensis MR-1. *Applied and Environmental Microbiology*. **77**, 4035–4041 (2011).

33. X. Li, H. Xu, F. Kong, R. Wang, A Cationic Metal-Organic Framework Consisting of Nanoscale Cages: Capture, Separation, and Luminescent Probing of Cr 2O 72–through a Single-Crystal to Single-Crystal Process. *Angew. Chem. Int. Ed.* **52**, 13769–13773 (2013).

34. H. Fei, C. S. Han, J. C. Robins, S. R. J. Oliver, A Cationic Metal–Organic Solid Solution Based on Co(II) and Zn(II) for Chromate Trapping. *Chem. Mater.* **25**, 647–652 (2013).

35. H.-R. Fu, Z.-X. Xu, J. Zhang, Water-Stable Metal–Organic Frameworks for Fast and High Dichromate Trapping via Single-Crystal-to-Single-Crystal Ion Exchange. *Chem. Mater.* **27**, 205–210 (2014).

36. D. Mohan, C. U. Pittman Jr, Activated carbons and low cost adsorbents for remediation of tri- and hexavalent chromium from water. *Journal of Hazardous Materials*. **137**, 762–811 (2006).

37. B. T. N. Pham, L. M. Lund, D. Song, Novel Luminescent Metal-Organic Frameworks [Eu 2L 3(DMSO) 2(MeOH) 2]·2DMSO·3H 2O and [Zn 2L 2(DMSO) 2]·1.6H 2O (L = 4,4′-Ethyne-1,2-diyldibenzoate). *Inorg. Chem.* **47**, 6329–6335 (2008).

38. D. Feng, Z-Y. Gu, J-R. Li, H-L. Jiang, Z. Wei, H-C. Zhou, Zirconium-Metalloporphyrin PCN-222: Mesoporous Metal-Organic Frameworks with Ultrahigh Stability as Biomimetic Catalysts. *Angew. Chem. Int. Ed.* **51**, 10307–10310 (2012).

39. S. S. Park, E. R. Hontz, L. Sun, C. H. Hendon, A. Walsh, T. van Voorhis, M. Dinca, Cation-Dependent Intrinsic Electrical Conductivity in Isostructural Tetrathiafulvalene-Based Microporous Metal–Organic Frameworks. *J. Am. Chem. Soc.* **137**, 1774–1777 (2015).

40. N. C. Burtch, H. Jasuja, K. S. Walton, Water Stability and Adsorption in Metal–Organic Frameworks. *Chem. Rev.* **114**, 10575–10612 (2014).

41. J. K. Fredrickson, J. M. Zachara, D. W. Kennedy, C. Liu, M. C. Duff, D. B. Hunter, A. Dohnalkova, Influence of Mn oxides on the reduction of uranium(VI) by the metal-reducing bacterium Shewanella putrefaciens, 1–16 (2002).

42. S. Kato, K. Hashimoto, K. Watanabe, Methanogenesis facilitated by electric syntrophy via (semi)conductive iron-oxide minerals. *Environmental Microbiology*. **14**, 1646–1654 (2011).

43. F. Liu, A-E. Rotaru, P. M Shrestha, N. S. Malvankar, K. P. Nevin, D. R. Lovley, Magnetite compensates for the lack of a pilin-associated c-type cytochrome in extracellular electron exchange. *Environmental Microbiology*. **17**, 648–655 (2014).

44. K. Guesh, C. A. D. Cauiby, A. Mayoral, M. Diaz-Garcia, M. Sanchez-Sanchez, Sustainable Preparation of MIL-100(Fe) and Its Photocatalytic Behavior in the Degradation of Methyl Orange in Water. *Crystal Growth & Design*. **17**, 1806–1813 (2017).

45. M. Sanchez-Sanchez, I. de Asua, D. Ruano, K. Diaz, Direct Synthesis, Structural Features, and Enhanced Catalytic Activity of the Basolite F300-like Semiamorphous Fe-BTC Framework. *Crystal Growth & Design*. **15**, 4498–4506 (2015).

46. J. Wang, J. Wan, Y. Ma, Y. Wang, M. Pu, Z. Guan, Metal–organic frameworks MIL-88A with suitable synthesis conditions and optimal dosage for effective catalytic degradation of Orange G through persulfate activation. *RSC Advances*. **6**, 112502–112511 (2016).

47. D. Baron, E. LaBelle, D. Coursolle, J. A. Gralnick, D. R. Bond, Electrochemical

measurement of electron transfer kinetics by Shewanella oneidensis MR-1. *J. Biol. Chem.* **284**, 28865–28873 (2009).

48. L. L. Stookey, Ferrozine---a new spectrophotometric reagent for iron. *Anal. Chem.* **42**, 779–781 (1970).

49. A. Coreno-Alonso, G. Cruz-Jimenez, L. Lopez-Martinez, G. E. Reyna-Lopez, F. J. Acevedo-Aguilar, A rapid, eco-friendly, and reliable microplate method for determination of Cr(VI). *Turk J Chem*. **41**, 420–425 (2017).

50. W. Jiang, Q. Cai, W. Xu, M. Yang, Y. Cai, D. D. Dionysios, K. E. O'Shea, Cr(VI) Adsorption and Reduction by Humic Acid Coated on Magnetite. *Environ. Sci. Technol.* **48**, 8078–8085 (2014).

51. W. Yin, Y. Li, J. Wu, G. Chen, G. Jiang, P. Li, J. Gu, H. Liang, C. Liu, Enhanced Cr(VI) removal from groundwater by Fe0-H2O system with bio-amended iron corrosion. *Journal of Hazardous Materials*. **332**, 42–50 (2017).

52. C. Ni, S. Liu, L. Cui, Z. Han, L. Wang, R. Chen, H. Liu, Adsorption performance of Cr(vi) onto Al-free and Al-substituted ferrihydrites. *RSC Advances*. **6**, 66412–66419 (2016).

53. M. Lu, X.-H. Guan, X.-H. Xu, D.-Z. Wei, Characteristic and mechanism of Cr(VI) adsorption by ammonium sulfamate-bacterial cellulose in aqueous solutions. *Chinese Chemical Letters*. **24**, 253–256 (2013).

54. T. Srinath, T. Verma, P. W. Ramteke, S. K. Garg, Chromium (VI) biosorption and bioaccumulation by chromate resistant bacteria. *Chemosphere*. **48**, 427–435 (2002).

55. A. Tytłak, P. Oleszczuk, R. Dobrowolski, Sorption and desorption of Cr(VI) ions from water by biochars in different environmental conditions. *Environ Sci Pollut Res*. **22**, 5985–5994 (2014).

56. X. Li, H. Xu, F. Kong, R. Wang, A Cationic Metal-Organic Framework Consisting of Nanoscale Cages: Capture, Separation, and Luminescent Probing of Cr 2O 72–through a Single-Crystal to Single-Crystal Process. *Angew. Chem. Int. Ed.* **52**, 13769–13773 (2013).

Acknowledgements

We thank Hazel Mohamedali, Riley Shuping, Gang Fan, and Michael Lucas for their experimental assistance. *S. oneidensis* strains Δ*bfe* and Δ*mtrC*Δ*omcA* were generously provided by Prof. Jeffrey Gralnick and *E. coli* MG1655 was generously provided by Prof. Lydia Contreras. We also thank Prof. Contreras for use of her imaging resources. We gratefully acknowledge the use of facilities within the core microscopy lab of the Institute for Cellular and Molecular Biology, University of Texas at Austin and within the X-Ray Diffraction Lab, University of Texas at Austin.

Author Contributions: S.K.S., C.M.D., and B.K.K conceived and designed the experiments.

S.K.S. and C.M.D. performed the experiments. S.K.S. performed the material synthesis and characterization. B.K.K. supervised the project. All authors contributed to data analysis and the writing of the manuscript. **Funding:** This work was partially supported by the Welch Foundation (Grant F-1929) and the National Science Foundation through the Center for Dynamics and Control of Materials: an NSF Materials Research Science and Engineering Center under Cooperative Agreement DMR-1720595. **Competing Interests:** The authors declare they have no competing interests. **Data availability:** All data needed to evaluate the conclusions of this paper are present in the paper and/or Supplementary Materials. Raw data are available from the Texas Data Repository.

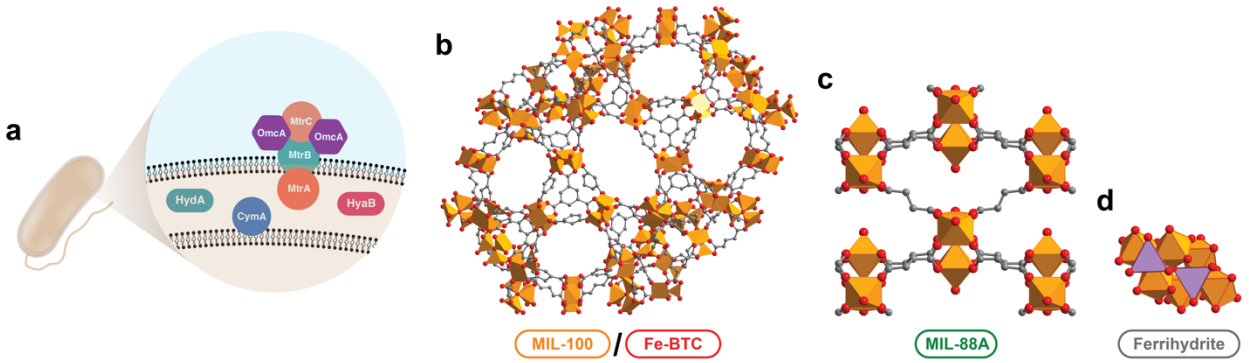

Figure 1. MR-1 reduction pathway and metal-organic framework structure. (a) The Mtr pathway by which *S. oneidensis* reduces both soluble and insoluble metal species(*1*). (b-d) The crystal structure of MIL-100/Fe-BTC (b,(*44*)), MIL-88A (c,(*46*)), and ferrihydrite (d,(*24*)). Fe-BTC does not have a known crystal structure (due to its amorphous nature) but it is analogous to MIL-100.

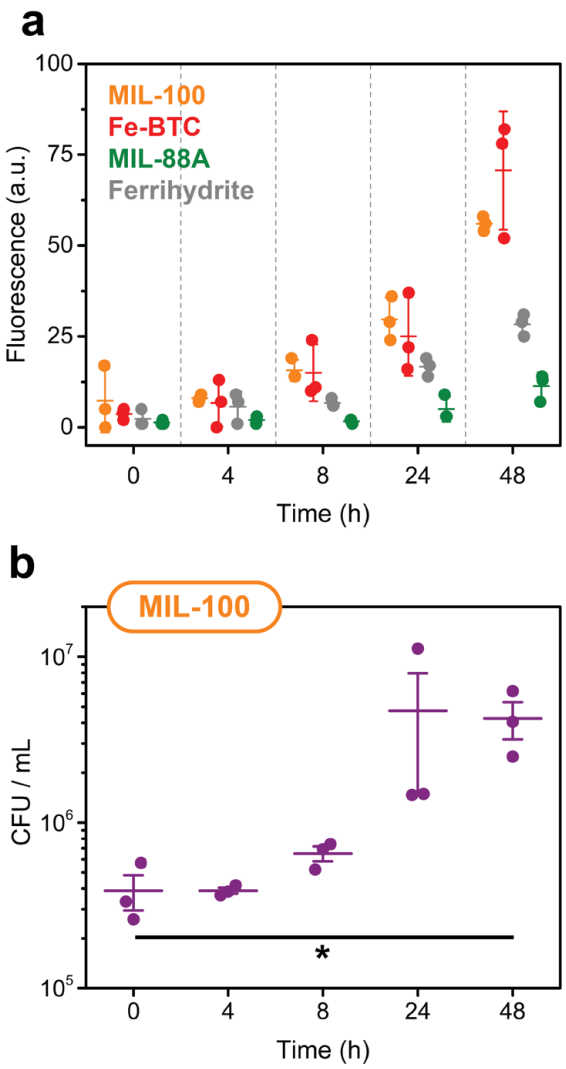

Figure 2. Growth of *S. oneidensis* MR-1 on metal-organic frameworks. (a) Background subtracted auto-fluorescence of MR-1 when cultured with MIL-100 (orange), Fe-BTC (red), MIL-88A (green), and ferrihydrite (grey) over 48 h. For both Fe-BTC and MIL-100, there is a significant difference between the auto-fluorescence of 24 h and 48 h ($p < 0.01$). Data show mean ± S.D. for three independent experiments. (b) CFU counts of MR-1 grown on MIL-100 over 48 h. Data show mean ± S.E. for three independent experiments. * $p < 0.05$.

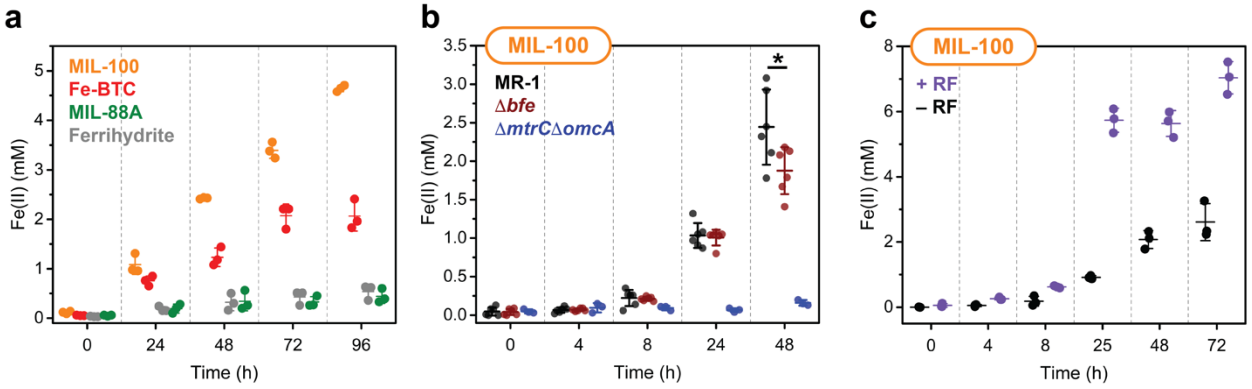

Figure 3. Reduction of metal-organic frameworks by *S. oneidensis*. (a) Reduction of MIL-100 (orange), Fe-BTC (red), MIL-88A (green), and ferrihydrite (grey) over 96 h. Data shown are mean ± S.D. for three independent experiments. (b) Reduction of MIL-100 by MR-1 (black), Δ*bfe* (burgundy), and Δ*mtrC*Δ*omcA* (blue) over 48 h. Data show mean ± S.D. for six independent experiments. (c) Reduction of MIL-100 by MR-1 with (purple) and without (black) exogenous 10 μM riboflavin supplementation. Data show mean ± S.D. for three independent experiments. * $p < 0.05$

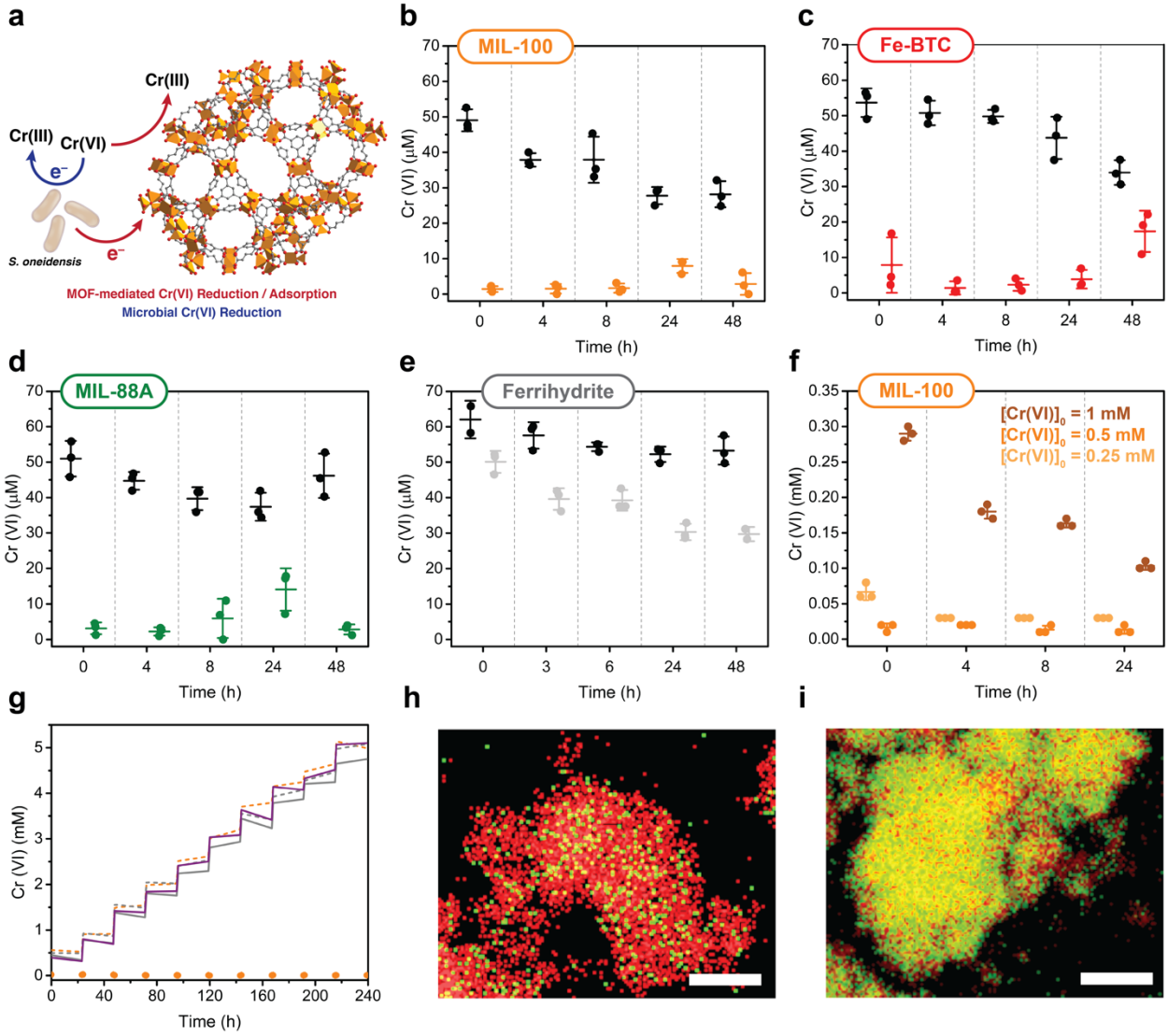

Figure 4. Cr(VI) removal in MR-1 reduced metal-organic frameworks. (a) Generalized scheme for Cr(VI) reduction by both MR-1 and a reduced metal-organic framework. (b-e) Cr(VI) removal by MR-1-reduced (b) MIL-100, (c) Fe-BTC, (d) MIL-88A, and (e) ferrihydrite when challenged with 70 μM Cr(VI). Abiotic samples for each material are shown in black. (f) Cr(VI) removal by MR-1-reduced MIL-100 when challenged with 0.25 mM, 0.5 mM, and 1 mM Cr(VI). (g) Cr(VI) removal in MR-1-reduced MIL-100 (orange), ferrihydrite (grey) and fumarate (purple) when challenged with ten cycles of 0.5 mM Cr(VI). Abiotic samples are shown as dashed lines. (h-i) EDX element mapping of (h) abiotic cycled MIL-100 and (i) MR-1-reduced and cycled MIL-100. Fe is shown in red and Cr is shown in green. Data show mean ± S.D. for three independent experiments.